Available online at www.sciencedirect.com
ScienceDirect
Journal of the European Ceramic Society 28 (2008) 159–167
www.elsevier.com/locate/jeurceramsoc

# Sintering behaviour of calcium phosphate filaments for use as hard tissue scaffolds

H.Y. Yang [a], S.F. Yang [a], X.P. Chi [a], J.R.G. Evans [a,*], I. Thompson [b], R.J. Cook [b], P. Robinson [b]

[a] *Department of Materials, Queen Mary, University of London, Mile End Road, London E1 4NS, UK*
[b] *GKT Dental Institute, Kings College, London SE1 9RT, UK*

Received 25 October 2006; received in revised form 20 April 2007; accepted 28 April 2007
Available online 1 August 2007

**Abstract**

Lattices consisting of hydroxyapatite (HA) and β-tricalcium phosphate (β-TCP) mixtures were prepared by extrusion freeforming to serve as bone substitute structures in which both shape and structural hierarchy are determined by computer control. Fine ceramic filaments were prepared from a non-aqueous, solvent-based, ceramic–polymer paste and sintered at temperatures from 1100 to 1300 °C. The characteristics of the sintered filaments were investigated because this determines the resulting microporosity and phase content while the higher levels of porosity are computer controlled. The effects of HA/β-TCP ratio and sintering temperature on the microstructure, density, shrinkage and final phase content were studied. These results provide a design reference for hard tissue engineering scaffolds built from these materials.


*Keywords:* Extrusion freeforming; Sintering; Biomedical applications; Apatite

## 1. Introduction

Sintered calcium phosphate ceramics based on hydroxyapatite (HA, $Ca_{10}(PO_4)_6(OH)_2$) and β-tricalcium phosphate (β-TCP, $Ca_3(PO_4)_2$) are the most prominent bone substitution materials among a wide range of calciferous candidates.[1–3] HA is similar to the carbonated apatite existing in natural bone but it shows limited resorption in vivo and is therefore often used in conjunction with TCP, which can be readily degraded in the body.[4] Biphase HA/TCP materials have been successfully used for osteoconduction and osteoinduction.[5,6] The pore structure of HA/TCP scaffolds is regarded as a main factor in promoting osteoinduction with the intention that the implanted porous ceramic will be progressively replaced by natural bone. Recent research on bone substitutes focuses on manufacturing methods that optimise the pore structure.[7,8] Essentially a structural hierarchy is sought in which fine pores (∼1 μm) are needed to provide dissolution and encourage cell adhesion and phenotype development, mid-range pores (10–100 μm) provide room for division and mineralization while large pores (>100 μm) provide corridors for vascularisation and internal mineralized bone formation.

Many methods have been used to manufacture porous ceramics. Conventional methods include the addition of a pore-former such as an organic material that burns away during firing[9] or a water soluble salt that can be leached out.[10] Slurry foaming methods involve the coating of a polymeric foam template followed by firing which removes the template[11] but tends to leave an internal defect in the foam struts.[12] Gel casting routes involve the direct polymerisation of foamed slurry.[13] Direct foaming of a polyurethane suspension produces reticulated ceramic foams.[14,15] In these methods, the foam structure is influenced by viscosity, surface tension and nucleation of voids but is not directly controllable. There is a tendency for the window diameter to be dependent on overall porosity.[15] The conflict is thus between strength, which is controlled largely by porosity[16] and the attainment of large pores to provide a vascular system that supplies and maintains an adequate mass transport of oxygen and nutrients to the cells and removes waste metabolites.

Clearly a hierarchical structure is needed and the application of rapid prototyping (RP) or solid freeform fabrication (SFF) to tissue engineering may be the most promising method for

* Corresponding author. Tel.: +44 20 7882 5501; fax: +44 20 8981 9804.
*E-mail address:* j.r.g.evans@qmul.ac.uk (J.R.G. Evans).

0955-2219/$ – see front matter © 2007 Elsevier Ltd. All rights reserved.
doi:10.1016/j.jeurceramsoc.2007.04.013

producing scaffolds with customised external shape and predefined and reproducible internal morphology.[17,18] In this way, complex internal geometrical features of scaffolds, such as pore size, porosity, pore size distribution and pathways for a vascular system, can be manufactured.

The present work uses direct extrusion freeforming in which a ceramic paste with a volatile solvent is extruded into filaments and hence into a lattice structure.[19,20] The ceramic powder is compounded with binder and solvent and, after extrusion from a nozzle, welds to the previous layers and solidifies. Welding is by growth of the contact area driven by surface energy decrease and resisted by viscosity. As successive layers are deposited, a 3D lattice is built which can have missing strands in order to leave large internal channels. The organic contents can be removed at the beginning of the sintering schedule. With fine extrusion (<100 μm), the hierarchical structure of bone substitute can be easily manufactured but the microporosity of ceramic filaments is controlled by the powder and the sintering temperature.

The characteristics of sintered HA, β-TCP and HA/β-TCP biphasic ceramics have been studied by many[21–25] and are considered to have superior chemical and physical properties, such as dissolution, mechanical properties and osteogenic activity in vivo, but the results differ from one investigation to another. This is partly because the purity and the fabrication methods of porous scaffolds differ. To control the characteristics of such HA/β-TCP scaffolds precisely in these new fabrication technologies, the microstructural features which are below the scale of computer control also need to be studied. In this work, the microstructure and constituents of the ceramic filaments with different HA/β-TCP ratios sintered at different temperatures were investigated to provide a general reference for lattice design for hard tissue engineering scaffolds.

## 2. Experimental details

### 2.1. Materials

Table 1 details the materials used. The hydroxyapatite ($Ca_{10}(PO_4)_6(OH)_2$, Grade P221 S, Plasma Biotal Ltd., UK) and β-tricalcium phosphate ($Ca_3(PO_4)_2$, Grade P228 S, Plasma Biotal Ltd., UK) powders were prepared by the manufacturer by calcining at 900 °C and milling in water for 96 h. Manufacturer's XRD data, confirmed in our laboratory, corresponded to the standards. The morphology and the particle size were assessed by scanning electron microscopy (SEM, JEOL JSM6300F, Japan) and specific surface area was measured by gas adsorption (BET, model 5100, Micromeritics, Norcross, GA, USA). Samples were heated to 200 °C for 3 h before BET measurement. Poly(vinyl butyral) (PVB), grade BN18 (Wacker Chemicals, Germany) was used as the binder with additions of a grade of poly(ethylene glycol) (PEG) that is liquid at ambient temperature ($M_{Wt}$ = 600, VWR, UK).

### 2.2. Preparation of samples

Mixtures of 75 wt.% PVB and 25 wt.% PEG600 were fully dissolved in propan-2-ol (GPR, VWR, UK). Independently, powder mixtures having HA contents of 25, 50, 75 and 100 wt.% were dispersed in propan-2-ol with an ultrasonic probe (IKA U200S, IKA Labortechnik Staufen, Germany) for 15 min. These were mixed to provide a ceramic/polymer mixture which has 60 vol.% ceramic powder based on the dry mass. These mixtures were placed on a roller table with zirconia media for 12 h. Partial drying was used to reach a solvent level suitable for extrusion with intermittent stirring and the final solvent content was measured by drying a sample to constant mass at 60 °C.

The pastes were loaded into a syringe (HGB81320 1 ml, Hamilton GB Ltd., Carnforth, UK) and driven by micro-stepper motors (50,000 steps/rev) supplied by ACP&D Ltd., Ashton-under-Lyne, UK, with a 64-1 reduction box driving 1 mm pitch ball screws (Automotion Ltd., Oldham, UK) over a three axis table (Parker Hannifin Automation, Dorset, UK). The extrusion dies of 80, 100, 150 and 300 μm diameter were purchased from Quick-OHM (Sapphire water-jet cutting nozzle, models 1708, 1710, 1715 and 1730, Germany). The table was driven by Labview software to form latticework patterns. Filaments of 100 mm length and 300 μm diameter were extruded and cut into 80 mm length for sintering. Discs of paste with 20 mm diameter and 2 mm thick were made for XRD. After drying, the extruded filaments and discs were heated in five groups at 5 °C/min to 1100, 1150, 1200, 1250 and 1300 °C with a 5 h dwell before furnace cooling to room temperature.

### 2.3. Characterization

The cross sections and surfaces of the filaments both sintered and unsintered were observed by scanning electron microscopy (SEM, JEOL 6300, Japan). The length changes before and after sintering were measured to provide linear shrinkage. The density and porosity of filaments were calculated by measuring the mass and diameter of the cross section of 80 mm long filaments, the diameters being measured by optical microscopy (Model BX60, Olympus, Japan) with a graticule. Ten samples at least were used for each test.

Table 1
Detail of materials

| | Grade | Source | Density (kg m$^{-3}$) |
|---|---|---|---|
| Hydroxyapatite | P221 S | Plasma Biotal Ltd., UK | 3156 |
| β-Tricalcium phosphate | P228 S | Plasma Biotal Ltd., UK | 3070 |
| Poly(vinyl butyral) | BN18 | Wacker Chemicals, Germany | 1100 |
| Poly(ethylene glycol) | $M_{Wt}$, 600 | VWR, UK | 1127 |
| Propan-2-ol | GPR | VWR, UK | 789 |

XRD analysis of the ceramic was recorded on a diffractometer (Model D5000, Siemens, Karlsruhe, Germany) using Cu Kα radiation. The step size was 0.02° $2\theta$ with a count time of 2.5 s. Phases were identified using the International Centre for Diffraction Data powder diffraction files (no. 9-432 for HAP, no. 9-169 for β-TCP, and no. 9-348 for α-TCP). Peaks (2 1 0) for HA and (0 2 10) for β-TCP were used to calculate the ratios of intensities.

## 3. Results and discussion

### 3.1. Extrusion freeforming of HA/TCP lattices

Two-phase calcium phosphate can be made from calcium deficient hydroxyapatites $Ca_{10-x}(PO_4)_{6-x}(HPO_4)_x(OH)_{2-x}$ with $0 \leq x \leq 1$. Such powders are precipitated by conventional wet chemical methods and decomposed into a mixture of hydroxyapatite and tricalcium phosphate by thermal treatment above 700 °C. In this study, to satisfy the medical requirements, medical grade hydroxyapatite and β-tricalcium phosphate powders were used directly to make two-phase calcium phosphate mixtures.

Both HA and TCP powders used here meet compositional specifications for surgical implantation (ASTM F1088 and ASTM F1185-88), the content of the trace metals being within the maximum allowable limits. The specific surface areas of the as-received HA and TCP powders were 13.1 and 5.3 $m^2/g$ measured by BET $N_2$ adsorption. Fig. 1 shows the morphologies of these powders. The HA powder consists of well-separated particles, but the TCP powder has larger agglomerates.

PVB was used as the binder on the basis of its adhesive properties and solubility in propan-2-ol. PEG 600 improves fluidity during extrusion. These additives allow flow, enhance welding, prevent shrinkage–cracking and allow handling. The dry volume fraction was 60%; if it exceeds 70%, the filaments do not plastically deform during building and the dried filaments are brittle. The polymer can also be used to act indirectly as a porogen by reducing packing efficiency and hence final density.

HA and TCP powders can be dispersed well in propan-2-ol whereas in water, they were more easily flocculated and tended to settle. The solvent content controls the extrusion process and changes the state by volatilising. If the solvent content is too low, more pressure is needed to extrude the paste and high viscosity results in inadequate weld formation. If too much solvent is used, the paste has a low yield stress, does not maintain its shape and tends to slump between base-layer filaments. For the extrusion of 300 μm filaments, the solvent content was about 25 vol.%.

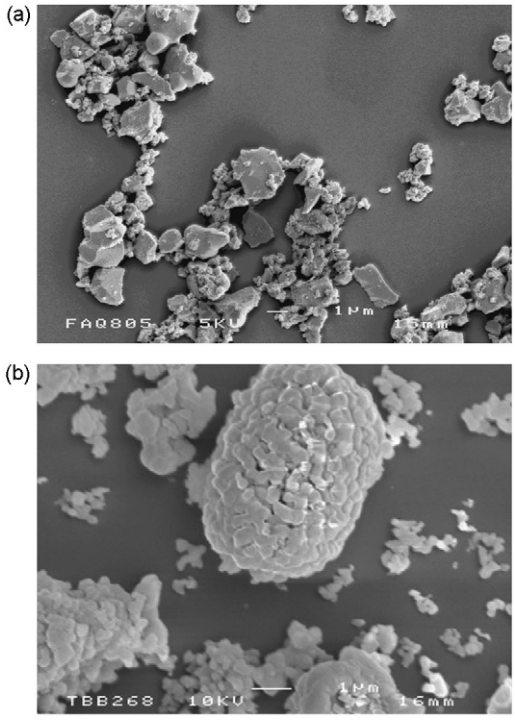


Fig. 1. SEM images of (a) HA and (b) TCP powders.

Lattices manufactured on the three-axis table using different nozzles are shown in Fig. 2 demonstrating the type of structures that are possible and that the higher levels of porosity in the hierarchy can be engineered by extrusion freeforming.

### 3.2. Microporosity

While the higher hierarchical levels of porosity in these scaffolds can be computer controlled through extrusion freeforming, the microstructure of the filaments, which affects dissolution in the prosthetic environment and the strength of filaments, is directly influenced by sintering temperature.

The surface microstructure of sintered filaments is presented to the body fluids and is the substrate upon which proteins adsorb and cells adhere to develop their phenotype. In contrast, the fracture surface, discussed below, demonstrates the extent and

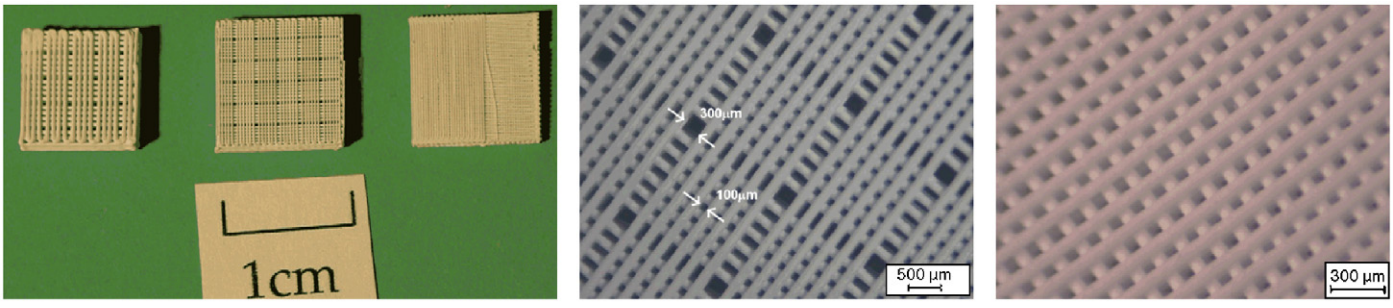


Fig. 2. Optical images of HA/TCP hard tissue scaffolds prepared by extrusion freeforming.

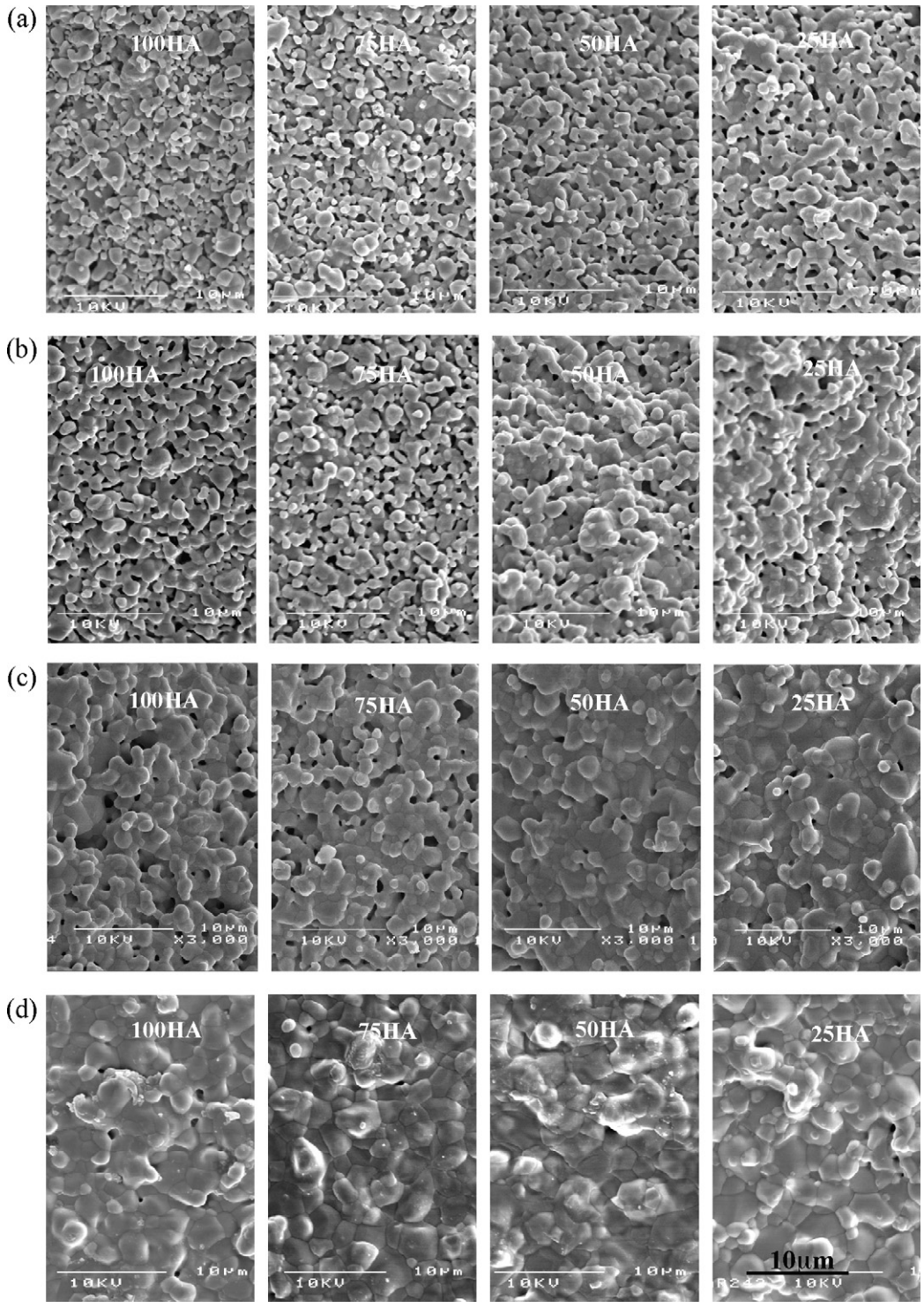


Fig. 3. SEM images of the surfaces of HA/TCP ceramic filaments sintered at different temperatures: (a) 1100 °C; (b) 1150 °C; (c) 1200 °C; (d) 1250 °C.

morphology of bulk porosity, which is relevant to cell development only when open porosity prevails but also influences mechanical properties. Fig. 3a shows the development of surface microstructure at a sintering temperature of 1100 °C as the composition becomes progressively β-TCP-rich. At 1100 °C, very little sintering has taken place. The particle size of β-TCP is larger and as its fraction increases, the overall microstructure appears somewhat coarser. The β-TCP sinters more readily than HA and produces more rounded particles at the surface even at this low temperature where HA particles retain their angularity.

At 1150 °C (Fig. 3b) the difference in surface structure is more pronounced: the surface of the β-TCP-rich sample is almost closed because of more rapid sintering, while the HA-rich surface shows rounding of particles and early stage neck formation. At 1200 °C (Fig. 3c), the surface of the β-TCP-rich sample

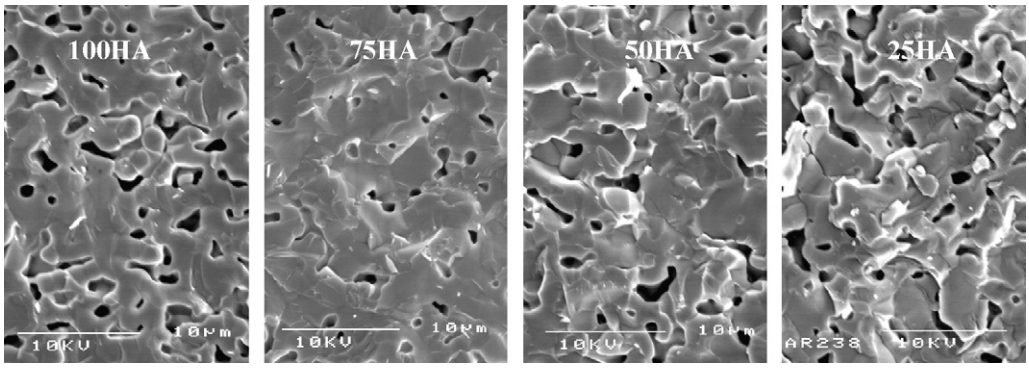


Fig. 4. Cross sections of filaments sintered at 1250 °C.

is almost completely sealed while the HA-rich sample surfaces still show many pores. Fig. 3d shows the samples sintered at 1250 °C wherein all filaments present sealed and smoothed surfaces to the biological environment.

This does not mean that the samples are fully dense; Fig. 4 shows the fracture section of filaments sintered at 1250 °C. Although the surfaces of the filaments appear sealed, the inner structure retains considerable closed porosity. As sintering temperature increases, the inner pores progressively disappear and the filament reaches high relative density. The density measurements shown below confirm the qualitative deductions from the microstructure.

### 3.3. Density

The porosity of sintered filaments was compared by measuring the density (Table 2) and converting to relative density, $\rho$, based on the theoretical density of individual mixtures as deduced from XRD measurements (*vide infra*). Using Rahaman's[26] designation of three sintering stages, all samples sintered at 1100 °C are in initial stage typified by $\rho < 0.65$, initial neck growth between particles and low mechanical strength. Conversely, when sintered above 1250 °C, all samples are at the final stage, having $\rho > 0.9$, with disappearance of closed porosity and more extensive grain growth. The transformation of a small amount of β-TCP to α-TCP is not taken into account in this calculation (this transformation causes a slight decrease in theoretical density), so relative densities of filaments sintered above 1250 °C are underestimated in the calculation and this effect is more pronounced in the β-TCP-rich samples. When sintered at 1150 and 1200 °C, the relative densities for most samples in the intermediate stage are in the range of $\rho = 0.65$–$0.9$, showing progressive disappearance of open porosity.

Although β-TCP-rich samples begin sintering at a lower temperature than HA-rich samples as deduced from microscopy, the relative density at 1100 °C is almost the same as the less sintered HA-rich samples because of the lower initial packing efficiency of the β-TCP-rich samples. It is well known that the arrangement of particles established by the shaping process affects the sintered structure and its defects.[27] It is expected that these sintered microstructures are affected by the drying process and the arrangement of particles that results from it and this is investigated by following the linear shrinkages at different stages of preparation.

### 3.4. Linear shrinkage

To fix the final lattice dimensions, the design file must compensate for the overall linear shrinkage, which takes place in two stages, drying and sintering. These two shrinkages, $S_1$ and $S_2$, and the total shrinkage $S$ are defined by

$$S_1 = \frac{L_0 - L_1}{L_0} \quad (1)$$

$$S_2 = \frac{L_1 - L_2}{L_1} \quad (2)$$

$$S = \frac{L_0 - L_2}{L_0} = S_1 + S_2 - S_1 S_2 \quad (3)$$

where $L_0$, $L_1$ and $L_2$ are the initial, dried and sintered filament lengths, respectively.

During drying, shrinkage occurs as solvent is lost from the polymer–solvent system in the pore structure. Particle centres approach, leaving a binary polymer–ceramic system with 60 vol.% powder as fixed by formulation decisions. This value was chosen to confer strength on the dry but unsintered lattice.

Table 2
Density of filaments (kg m$^{-3}$), and relative density[a] (shown in parentheses), with different HA/TCP ratio sintered at different temperatures

| | 1300 °C | 1250 °C | 1200 °C | 1150 °C | 1100 °C |
|---|---|---|---|---|---|
| 100HA | 3020 ± 110 (0.96) | 2900 ± 100 (0.92) | 2420 ± 90 (0.77) | 2170 ± 80 (0.69) | 2030 ± 70 (0.64) |
| 75HA | 3060 ± 40 (0.98) | 3010 ± 30 (0.96) | 2500 ± 30 (0.80) | 2140 ± 30 (0.68) | 2000 ± 20 (0.64) |
| 50HA | 2930 ± 50 (0.94) | 2860 ± 50 (0.92) | 2660 ± 50 (0.88) | 2110 ± 40 (0.68) | 1970 ± 30 (0.63) |
| 25HA | 2820 ± 40 (0.92) | 2770 ± 30 (0.90) | 2540 ± 30 (0.87) | 2250 ± 30 (0.73) | 1940 ± 30 (0.63) |

[a] Deduced from theoretical density calculated from phase composition in Table 4 and neglecting conversion to α-TCP.

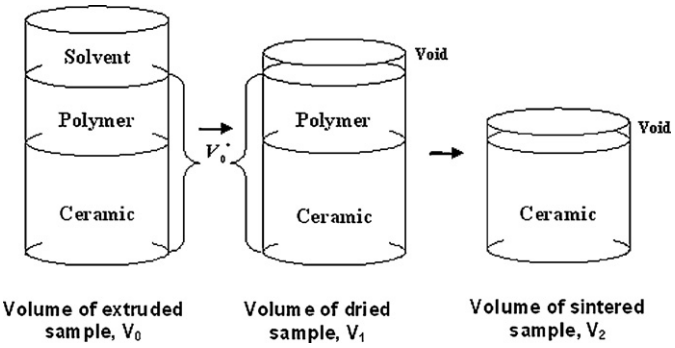


Fig. 5. Schematic illustration of volume changes of the filament after drying and sintering.

However, because this formulation is near the limit of powder loading, particle contact may occur before drying is complete and the binary system may become a ternary composed of polymer, ceramic and porosity.

Fig. 5 shows the volume changes of a filament after drying and sintering. Since the drying process started immediately after the filament emerged from the die, it is impossible to measure the length change, so the initial shrinkage was obtained indirectly. Supposing that this shrinkage is isotropic, the linear shrinkage is related to volume fractions as follows:

$$S_1 = \frac{L_0 - L_1}{L_0} = 1 - \sqrt[3]{\frac{V_1}{V_0}} \tag{4}$$

where $V_1$ is the actual volume of filaments after drying and can be calculated from

$$V_1 = \frac{V_0^* \rho_0^*}{\rho_1} \tag{5}$$

where $V_0^*$ is the volume of the fully dense ceramic and polymer binary as shown in Fig. 5. $\rho_0^*$ is the calculated theoretical density of the ceramic and polymer composite and $\rho_1$ is the actual density of the dried ceramic and polymer filaments with different HA/β-TCP ratios. Here, $\rho_1 \leq \rho_0^*$ because full packing of the binary system may not be obtained. For the filament of length $l$ extruded by a nozzle of radius $r_0$, after drying the measured mass is $W_l$ and then $\rho_1$ is calculated from

$$\rho_1 = \frac{W_l}{V_l} = \frac{W_l}{l\pi r^2} = \frac{W_l}{l\pi r_0^2 (1 - S_1)^2} \tag{6}$$

Inserting $\rho_1$ into Eq. (5) and inserting $V_l$ into Eq. (4), we find

$$S_1 = 1 - \frac{l\pi r_0^2 \rho_0^* V_0^*}{W_l V_0} \tag{7}$$

where $V_0^*/V_0$ is the volume fraction of the polymer and ceramic in the paste which was measured before extrusion. So by measuring the mass of a dried filament with fixed length $W_l$, we obtain the drying shrinkage.

Table 3 gives the drying linear shrinkage for different samples. With an increase of β-TCP content, the linear shrinkage of the filament after extrusion decreases indicating a lower packing efficiency. From the SEM (Fig. 6) it can be seen that for 100HA, the dried filament (polymer and ceramic are shown here) has a smooth and dense surface, but for the 25HA, the surface is rough and porous indicating that the pore structure is not saturated by the polymer phase.

The sintering shrinkage has two contributions: loss of polymer in the early stages and loss of porosity at the sintering temperature. Using dried filaments with $L_1 = 80$ mm, the length of the filaments $L_2$ were measured, and sintering shrinkages were calculated by Eq. (2) using five samples for each experiment. The error is due to measurement precision in length, which is about ±0.5 mm. Table 3 also shows the shrinkages of the different compositions sintered at different temperatures. For each temperature there is a systematic increase in sintering shrinkage with increasing β-TCP content and a systematic increase with sintering temperature.

The total linear shrinkages were calculated from the drying and sintering shrinkages (Eq. (3)), and results are shown

Table 3
Linear shrinkage of filaments after drying, $S_1$, and sintering linear shrinkage, $S_2$, of different sintering temperatures

| Samples | $S_1$ | 1300 °C | 1250 °C | 1200 °C | 1150 °C | 1100 °C |
|---|---|---|---|---|---|---|
| 100HA | 0.068 | 0.162 | 0.138 | 0.062 | 0.038 | 0.012 |
| 75HA | 0.054 | 0.169 | 0.144 | 0.075 | 0.056 | 0.025 |
| 50HA | 0.033 | 0.175 | 0.156 | 0.15 | 0.088 | 0.05 |
| 25HA | 0.022 | 0.188 | 0.162 | 0.162 | 0.106 | 0.056 |

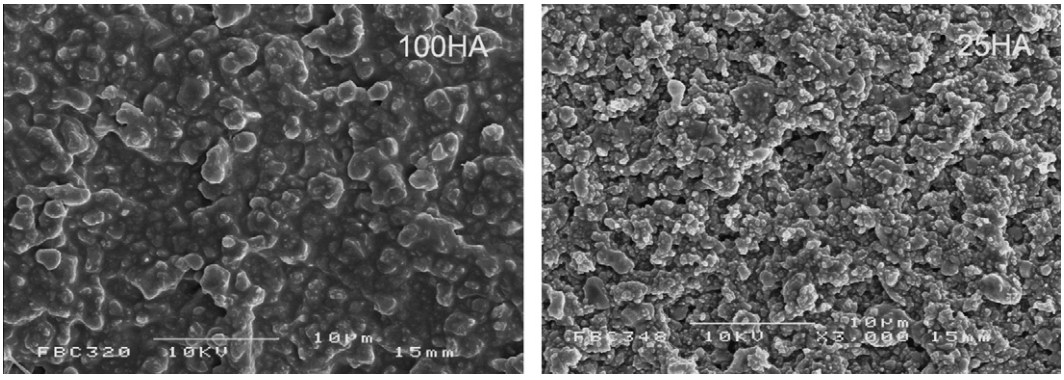


Fig. 6. SEM images of surfaces of dried filaments.

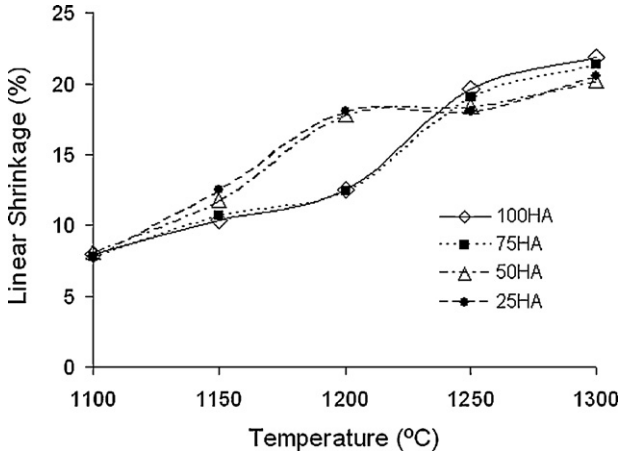


Fig. 7. Linear shrinkages of HA/β-TCP filaments sintered at different temperatures.

in Fig. 7. The obvious difference is that HA-rich samples sinter more slowly than the β-TCP-rich samples at a sintering temperature of 1200 °C and below, but the shrinkages at 1250 and 1300 °C are similar. Consistent with the density results (Table 2), β-TCP-rich samples have higher shrinkage during sintering but the total shrinkage may be still no more than that of the HA-rich samples due to the lower starting density.

The length to diameter shrinkage ratio may differ from unity if there is particle shape anisotropy. This ratio can be deduced from the shrinkage of the whole lattice (Fig. 2) in the *X*–*Y* plane and the shrinkage in the *Z* plane, the latter representing the diametral shrinkage. Here the ratio was better than 0.95, so the particles were taken as isotropic to simplify the calculation.

From the shrinkage results, the design dimensions needed to obtain the manufactured and sintered dimensions can be calculated. For example, when using 75HA/25β-TCP materials to make 10 mm × 10 mm × 7 mm products with a sintering temperature of 1150 °C, the manufacturing dimensions are 11 mm × 11 mm × 7.7 mm, but for a sintering temperature of 1250 °C, they are 12.3 mm × 12.3 mm × 8.6 mm.

### 3.5. Phase composition

After sintering, not only the morphology but also the phase composition changed depending on the sintering temperature and phase purity. The phase contents were investigated by XRD. Construction of a calibration curve for phase analysis is a simple and well-tried method[28–32] although software is now available for a more direct method[33] Toth et al.[28] used relative peak heights to calculate the HA content by the intensity fraction of the $I_{100}$ peak, although this can be in error as much as 10% for the ratio of HA/TCP. Raynaud et al.[32] simplified the calibration curve into a series of linear equations for different HA/TCP ratios. In this way, a high accuracy can be obtained. In this study, a calibration curve was given by a series HA/β-TCP mixtures with different HA/TCP ratios.

An XRD pattern for a two-phase powder mixture containing 75 wt.% HA and 25 wt.% β-TCP is shown in Fig. 8a. From this

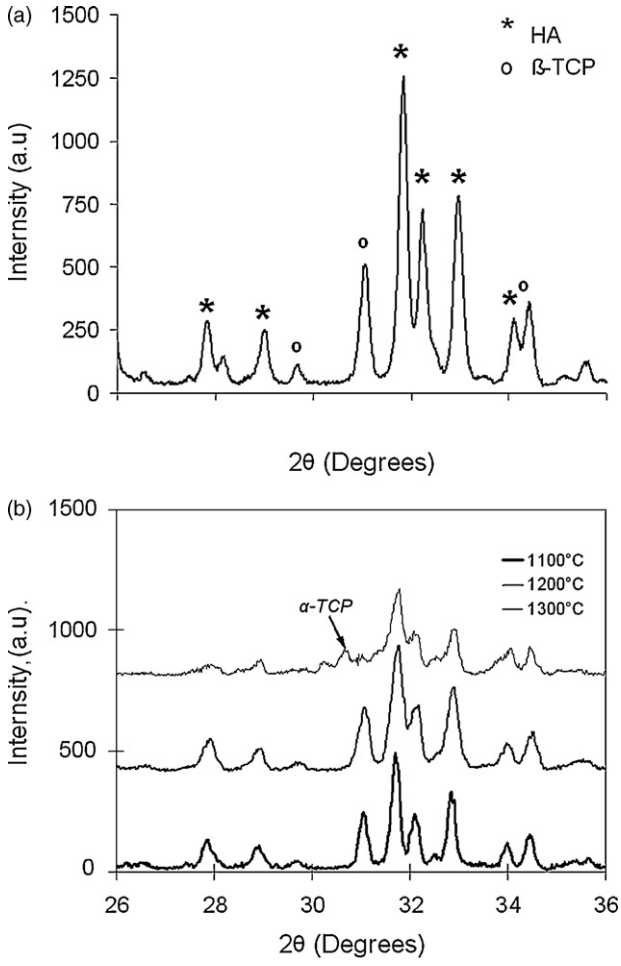


Fig. 8. XRD traces for 75HA (a) powder and (b) sintered samples.

pattern, avoiding partial peak superposition, the most appropriate peaks for quantitative analysis correspond to the plane (2 1 0) at $2\theta = 29°$ for HA and to the plane (0 2 10) at $2\theta = 31°$ for β-TCP. These peaks have been used previously for quantitative interpretation and it is claimed to be possible to detect β-TCP amounts as low as 0.5%.

Fig. 8b shows that after sintering, the intensity of the β-TCP increased. When sintered at 1250 °C, there were clear α-TCP peaks for 25HA and 50HA and 75HA. When sintered at 1300 °C, more α-TCP was produced, even for 100HA. According to Zhou et al.,[34] pure synthetic HA is stable when it is sintered in dry or wet air for long times below 1200 °C and decomposes into TCP above 1200 °C. But for the samples being tested, some β-TCP was observed in the 100HA samples sintered at 1100 °C and above. A small amount of Ca-deficient hydroxyapatite (DHA), $Ca_{10-z}(HPO_4)_z(PO_4)_{6-z}(OH)_{2-z}$ may be present in the HA powder which may have been produced during milling and prolonged storage as a slurry. DHA has a similar crystal structure and identical XRD pattern (JCPD card no. 46-905) to HA making it difficult to detect when assessing phase purity by XRD. It can decompose to yield some β-TCP and water at temperatures above 800 °C according to Eq. (8) due to Monma et al.[35] which was slightly modified by Mortier

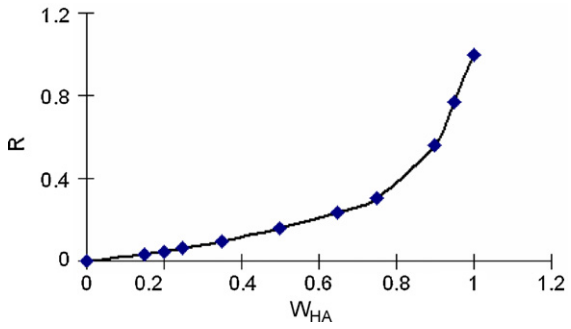


Fig. 9. Calibration curve of intensity ratio vs. HA weight fraction.

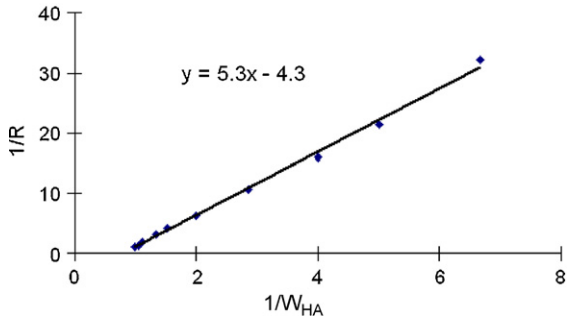


Fig. 10. Plot of $1/R$ against reciprocal HA weight fraction showing linearity.

et al.[36]:

$$Ca_{10-z}(HPO_4)_z(PO_4)_{6-z}(OH)_{2-z} \rightarrow (1-z)Ca_{10}(PO_4)_6(OH)_2 + 3zCa_3(PO_4)_2 + zH_2O \quad (8)$$

The intensity ratio of the peaks for HA and TCP is defined as follows:

$$R = \frac{I_{HA}}{I_{HA} + I_{TCP}} \quad (9)$$

If intensity is proportional to the weight fraction of the analyzed phase, $R$ can be expressed as

$$R = \frac{I^0_{HA} W_{HA}}{I^0_{HA} W_{HA} + I^0_{TCP} W_{TCP}} = \frac{1}{1 + (I^0_{TCP}/I^0_{HA})((1 - W_{HA})/W_{HA})} \quad (10)$$

Here $I^0_{HA}$ and $I^0_{TCP}$ are constants, and $W_{HA}$ is the weight fraction of HA in the two-phase mixture. This relation can be rewritten as follows:

$$\frac{1}{R} = A\frac{1}{W_{HA}} - A + 1 \quad (11)$$

where $A$ is a constant. This should provide a linear relationship between $1/R$ and $1/W_{HA}$, in which $A = I^0_{TCP}/I^0_{HA}$.

The value of $A$ was found from the calibration curve measured with HA and β-TCP powder mixtures. This ratio is plotted for 10 compositions individually prepared by weighing to give a calibration curve (Fig. 9) similar to that obtained by Raynaud et al.[32] Because of conversion of some HA to β-TCP at 1100 °C, a new batch of HA powder from the same manufacturer was taken and, after confirming the purity and stability of the powder by sintering at 1200 °C and inspecting the X-ray trace, the calibration curve was repeated. The two curves were co-incident.

The calibration curve produced from weighed mixtures of the starting powders using the data from Fig. 9 is shown in Fig. 10 as a curve of $1/R$ versus $1/W_{HA}$. The fitted curve has a slope of $A = 5.3$ and an intercept of 4.3, with a correlation coefficient of $r = 0.99$. Inserting this constant in Eq. (11), the phase composition of samples sintered at different temperatures can be calculated, and these are shown in Table 4. This quantitative phase analysis cannot be used for samples with α-TCP because of the overlapping of peaks, and the error may be significant when the HA weight fraction is less than 0.2.

Table 4
HA weight fraction of the sintered materials[a]

| Sample | 1250 °C | 1200 °C | 1150 °C | 1100 °C |
|---|---|---|---|---|
| 100HA | 0.851 | 0.832 | 0.841 | 0.849 |
| 75HA | – | 0.651 | 0.644 | 0.675 |
| 50HA | – | 0.36 | 0.365 | 0.369 |
| 25HA | – | 0.141 | 0.153 | 0.157 |

[a] Deduced from XRD; results are averages of two samples.

The results (Table 4) show that HA decomposed into β-TCP from 1100 °C, which indicates that the batch of HA milled and stored as slurry as in this experiment is not fully stable. When the TCP content was high (≥50 wt.%), the proportion of decomposed HA was greater than that in the HA-rich samples. Thus conversion was about 15% for 100HA and 75HA but rose to 27% and 40% for 50HA and 25HA, respectively. This coincides with the hypothesis of Kivrak et al.[37]. Their results show that the presence of TCP phase in composite powders stimulates the further decomposition of the HA phase through dehydroxylation. On the other hand, the sintered ceramic mixtures were not significantly affected by increasing the sintering temperature from 1100 to 1200 °C.[37]

The porosity, β-TCP and α-TCP contents affect the dissolution behaviour, strength and biological properties of filaments. So the HA/β-TCP ratio and the sintering temperature need to be decided according to the biological requirements. This in turn determines the shrinkage and hence the design data to give a lattice of specified dimensions.

## 4. Conclusion

The micro-extrusion freeforming process can produce scaffolds with customised external shape and predefined and reproducible hierarchical levels of internal structure. At the lower level, pore size, porosity and pore size distribution at the sub-micron level can be controlled by sintering at different temperatures. Drying shrinkage was investigated to understand the packing efficiency of the intermediate polymer–ceramic composite, which affects the sintered microstructure. The drying shrinkage decreased with increasing β-TCP content while the sintering shrinkage increased with increasing sintering temperature and β-TCP content. A shrinkage calibration needs to be

made before planning a fabrication process in order to meet dimensional tolerances. The porosity of the ceramic filaments can be varied from fully dense to about 35% by controlling sintering temperature. The composition of the ceramic product changes depending on the stability of the HA, the ratio of HA/β-TCP and the sintering temperature. The procedure provides a route for lattices with suitable characteristics such as porosity, strength and dissolution for clinical applications.

## Acknowledgement

The authors are grateful to the Engineering and Physical Sciences Research Council (EPSRC) for supporting this work under grant numbers GR/S57068 and GR/S52636.

## References

1. Monchau, F., Lefevre, A., Descamps, M., Belquin-myrdycz, A., Laffargue, P. and Hildebrand, H. F., In vitro studies of human and rat osteoclast activity on hydroxyapatite, beta-tricalcium phosphate, calcium carbonate. *Biomol. Eng.*, 2002, **19**, 143–152.
2. Fujita, R., Yokoyama, A., Kawasaki, T. and Kohgo, T., Bone augmentation osteogenesis using hydroxyapatite and beta-tricalcium phosphate blocks. *J. Oral. Maxillofac. Surg.*, 2003, **61**, 1045–1053.
3. Herath, H. M., Silvio, L. D. and Evans, J. R. G., Porous hydroxyapatite ceramics for tissue engineering. *J. Appl. Biomater. Biomech.*, 2005, **3**, 192–198.
4. Chu, T. M. G., Orton, D. G., Hollister, S. J., Feinberg, S. E. and Halloran, J. W., Mechanical and in vivo performance of hydroxyapatite implants with controlled architectures. *Biomaterials*, 2002, **23**, 1283–1293.
5. Kurashina, K., Kurita, H., Wu, Q., Ohtsuka, A. and Kobayashi, H., Ectopic osteogenesis with biphasic ceramics of hydroxyapatite and tricalcium phosphate in rabbits. *Biomaterials*, 2002, **23**, 407–416.
6. Yuan, H., Kurashina, K., de Bruijn, J. D., Li, Y., de Groot, K. and Zhang, X. D., A preliminary study on osteoinduction of two kind of calcium phosphate ceramic. *Biomaterials*, 1999, **20**, 1799–1806.
7. Wilson, C. E., de Bruijn, J. D., van Blitterswijk, C. A., Verbout, A. J. and Dhert, W. J. A., Design and fabrication of standardized hydroxyapatite scaffolds with a defined macro-architecture by rapid prototyping for bone-tissue-engineering research. *J. Biomed. Mater. Res.*, 2004, **68A**, 123–132.
8. Hollister, S. J., Porous scaffold design for tissue engineering. *Nat. Mater.*, 2005, **4**, 518–524.
9. Karageorgiou, V. and Kaplan, D., Porosity of 3D biomaterial scaffolds and osteogenesis. *Biomaterials*, 2005, **26**, 5474–5491.
10. Pradhan, M. and Bhargava, P., Effect of sucrose on fabrication of ceramic foams from aqueous slurries. *J. Am. Ceram. Soc.*, 2005, **88**, 216–218.
11. Peng, H. X., Fan, Z., Evans, J. R. G. and Busfield, J. J. C., Microstructure of ceramic foams. *J. Eur. Ceram. Soc.*, 2000, **20**, 807–813.
12. Lange, F. F. and Miller, K. T., Low density ceramics fabricated from reticulated polymer substrates. *Adv. Ceram. Mater.*, 1987, **2**, 827–831.
13. Sepulveda, P. and Binner, J. G. P., Processing of cellular ceramics by foaming and in situ polymerisation of organic monomers. *J. Eur. Ceram. Soc.*, 1999, **19**, 2059–2066.
14. Powell, S. J. and Evans, J. R. G., The structure of ceramic foams prepared from polyurethane ceramic suspensions. *Mater. Manuf. Proc.*, 1995, **10**, 757–771.
15. Ebaretonbofa, E. and Evans, J. R. G., High porous foam scaffolds for bone substitute. *J. Porous Mater.*, 2002, **9**, 257–263.
16. Gibson, L. J. and Ashby, M. F., *Cellular Solids: Structure and Properties* (*2nd ed.*). Cambridge University Press, Cambridge, UK, 1997.
17. Yang, S., Leong, K. F., Du, Z. and Chua, C. K., The design of scaffolds for use in tissue engineering. Part II. Rapid prototyping techniques. *Tissue Eng.*, 2002, **8**, 1–12.
18. Seitz, H., Rieder, W., Irsen, S., Leukers, B. and Tille, C., Three-dimensional printing of porous ceramic scaffolds for bone tissue engineering. *J. Biomed. Mater. Res.*, 2005, **74B**, 782–788.
19. Gomes de Sousa, F. C. and Evans, J. R. G., Sintered hydroxyapatite latticework for bone substitute. *J. Am. Ceram. Soc.*, 2003, **86**, 517–519.
20. Yang, H. Y., Yang, S., Chi, X. P. and Evans, J. R. G., Fine ceramic prepared by extrusion freeforming. *J. Biomed. Mater. Res.*, 2006, **79B**, 116–121.
21. Raynaud, S., Champion, E., Bernache-Assollant, D. and Thomas, P., Calcium phosphate apatites with variable Ca/P atomic ratio. I. Synthesis, characterisation and thermal stability of powder. *Biomaterials*, 2002, **23**, 1065–1072.
22. Raynaud, S., Champion, E. and Bernache-Assollant, D., Calcium phosphate apatites with variable Ca/P atomic ratio. II. Calcination and sintering. *Biomaterials*, 2002, **23**, 1073–1080.
23. Raynaud, S., Champion, E. and Bernache-Assollant, D., Calcium phosphate apatites with variable Ca/P atomic ratio. III. Mechanical properties and degradation of hot pressed ceramics. *Biomaterials*, 2002, **23**, 1081–1089.
24. Habibovic, P., Yuan, H. P., Van der Valk, C. M., Meijer, G., van Blitterswijk, C. A. and de Groot, K., 3D microenvironment as essential element for osteoinduction by biomaterials. *Biomaterials*, 2005, **26**, 3565–3575.
25. Rangavittal, N., Landa-Canovas, A. R., Gonzales-Calbet, J. M. and Vallet-Regi, M., Structural study and stability of hydroxyapatite and β-tricalcium phosphate: two important bioceramics. *J. Biomed. Mater. Res.*, 2000, **51**(4), 660–668.
26. Rahaman, M. N., *Ceramic Processing and Sintering*. Marcel Dekker, New York, 2003, p. 486.
27. Evans, J. R. G., Particle contact before firing. *J. Eur. Ceram. Soc.*, 1997, **17**, 161–169.
28. Toth, J. M., Hirthe, W. M., Hubbard, W. G., Brantley, W. A. and Lynch, K. L., Determination of the ratio of HA/TCP mixtures by X-ray diffraction. *J. Appl. Biomater.*, 1991, **2**, 37–40.
29. Meganck, J. A., Baumann, M. J., Case, E. D., McCabe, L. R. and Allar, J. N., Biaxial flexure testing of calcium phosphate bioceramics for use in tissue engineering. *J. Biomed. Mater. Res.*, 2005, **72A**, 115–126.
30. Bouler, J. M., LeGeros, R. Z. and Dalculsi, G., Biphasic calcium phosphates: influence of three synthesis parameters on the HA/β-TCP ratio. *J. Biomed. Mater. Res.*, 2000, **51**, 680–684.
31. Zou, P., Ji, X. Y. and Zhang, X. L., Preparation and properties of β-TCP/HA biphase calcium phosphate powder. *J. Sichuan. Univ. (Nat. Sci. Ed.)*, 1996, **33**, 150–154.
32. Raynaud, S., Champion, E., Bernache-Assollant, D. and Laval, J. P., Determination of calcium/phosphorous atomic ratio of calcium phosphate apatite using X-ray diffractometry. *J. Am. Ceram. Soc.*, 2001, **84**, 359–366.
33. Okazaki, M., Taira, M. and Takahashi, J., Rietveld analysis and Fourier maps of hydroxyapatite. *Biomaterials*, 1997, **18**, 795–799.
34. Zhou, J. M., Zhang, X. D., Chen, J. Y., Zeng, S. X. and de Groot, K., High temperature characteristics of synthetic hydroxyapatite. *J. Mater. Sci.: Mater. Med.*, 1993, **4**, 83–85.
35. Monma, H., Ueno, S. and Kanazawa, T., Properties of hydroxyapatite prepared by the hydrolysis of tricalcium phosphate. *J. Chem. Technol. Biotechnol.*, 1981, **31**, 15–24.
36. Mortier, A., Lemaitre, J. and Rouxhet, P. G., Temperature-programmed characterization of synthetic calcium-deficient phosphate apatites. *Thermochim. Acta*, 1989, **143**, 265–282.
37. Kivrak, N. and Cuneyt Tas, A., Synthesis of calcium hydroxyapatite–tricalcium phosphate (HA–TCP) composite bioceramic powders and their sintering behavior. *J. Am. Ceram. Soc.*, 1998, **81**, 2245–2252.